

Estimation of elastic contrasts in a layered model from seismic *PS-to-PP* amplitude ratios

Nils Maercklin and Aldo Zollo

RISSC, Dipartimento di Scienze Fisiche, Università degli Studi di Napoli Federico II, Via Diocleziano 328, 80124 Napoli, Italy. E-mail: maercklin@na.infn.it

Accepted 2009 July 29. Received 2009 July 29; in original form 2008 June 23

SUMMARY

We present a method to estimate seismic velocity and density contrasts at a given interface in a 1-D layered model using *PS-to-PP* reflection amplitude ratios. The velocity structure above the reflector is constrained by traveltimes modelling, and the amplitude ratios are determined using the same source–receiver pair for the measured *PP* and *PS* amplitudes (common-offset geometry). Thereby, source and receiver site effects are cancelled, and the remaining propagation effects are included in the ray theoretical forward modelling of theoretical *PS-to-PP* ratios. A minimization of the least-squares misfit between observed and modelled ratios provides the remaining elastic parameters below the reflector of interest (*P* velocity, *P-to-S* velocity ratio, density). 1-D examples and a 2-D synthetic case study with a dipping reflector and a laterally varying overburden demonstrate the possibilities and limitations of the method. An application of the method to a 0.6 km deep reflector below the Campi Flegrei caldera, Italy, reveals a strong contrast with a *P*-velocity increase from less than 2 to 3.5 km s⁻¹ and a decrease of the *P-to-S* velocity ratio from 3.6 to 1.75. The proposed *PS-to-PP* amplitude ratio analysis is applicable for wide-angle seismic reflection data, especially when strong elastic parameter contrasts are expected and when source amplitudes or site effects are poorly known.

Key words: Controlled source seismology; Body waves; Acoustic properties.

1 INTRODUCTION

Seismic reflection amplitudes carry information on the elastic parameter contrasts at subsurface reflectors, and the estimated elastic parameters can be related to the rock type, porosity and fluid or gas content through empirical relationships and rock physics modelling (e.g. Avseth *et al.* 2005). Analyses of seismic reflection amplitude variations with source–receiver offset (AVO) or incident angle (AVA) are standard tools in seismic exploration to estimate these contrasts (Ostrander 1984; Castagna & Smith 1994; Hilterman 2001). Typically, these methods are applied to the amplitudes of *P-to-P* reflected waves, and often they employ linearized approximations to the Zoeppritz (1919) equations describing the reflection amplitude variation with incidence angle (see e.g. Aki & Richards 2002). These approximations are generally applied for small incidence angles (small offsets) only, and they assume weak elastic contrasts at the reflector. Some modifications are required to extend the approximate equations to the post-critical range of incidence angles (Downton & Ursenbach 2006), which in turn can provide more reliable estimates of seismic velocity and density contrasts.

The relationships between physical rock properties and *P*-wave seismic data are highly non-unique, but an additional analysis of *S*-wave data may increase the ability to extract lithology information and fluid effects from seismic data, because the effective shear modulus of porous rocks is not strongly affected by the fluid or gas

content of the pores (e.g. Xu & Bancroft 1997; Veire & Landrø 2006). The pore fill has only a minor influence on the effective *S*-wave velocity because of the related change in density and changes in the grain boundary contacts. Margrave *et al.* (2001) describe the joint inversion of *P-to-P* reflected (*PP*) and *P-to-S* converted (*PS*) wave amplitudes using a weighted stacking technique. In other joint inversion methods approximated linear expressions for *PP* and *PS* reflection coefficients are solved simultaneously for velocity and density contrasts at a reflector (Veire & Landrø 2006), or the inversion of reflection coefficients is formulated in a non-linear Bayesian framework (Rabben *et al.* 2008). Instead of approximations and numerical solutions for *PP*- and *PS*-AVA joint inversion, Kurt (2007) uses analytical expressions of the Zoeppritz equations combined with a bootstrapping approach to find the most likely estimates of bulk moduli, Poisson's ratios and densities in a two-layer model.

Standard AVO or AVA methods are applied to the reflection coefficients, and therefore source, receiver and propagation effects must be removed from the seismic data before the analysis. For example, a geometrical spreading correction may be applied, and reflection amplitudes may be normalized by the zero-offset amplitude in case of *PP* data. Alternatively, the use of amplitude ratios instead of absolute reflection coefficients can eliminate or reduce some of the propagation and site effects. Already Zoeppritz *et al.* (1912) studied amplitude ratios between reflected and direct *P* waves from distant earthquakes to derive seismic velocities within

the Earth. Later, Ibrahim (1971) obtained seismic properties of the Earth's core–mantle boundary from *PcP*-to-*P* ratios of teleseismic recordings. More recently, Auger *et al.* (2003) estimated the seismic velocities below a mid-crustal reflector using ratios between *PS*-converted and first-arrival *P* waves from a controlled-source experiment. Iidaka *et al.* (2004) and Sato *et al.* (2009) applied a similar technique to *PP*-reflected waves from the crust–mantle boundary. Besides that, Meissner & Hegazy (1981) proposed the analysis of *PP*-to-*SS* reflection coefficient ratios to characterize hydrocarbon reservoirs, and Li *et al.* (2006) used post-stack *PS*-to-*PP* amplitude ratios to delineate gas reservoirs in volcanic rocks.

Here we introduce an AVO method that utilizes *PS*-to-*PP* amplitude ratios from wide-angle, three-component pre-stack seismic sections and dynamic ray modelling. For a given source–receiver offset, the *PS*-to-*PP* ratio depends mostly on just the elastic parameters at the reflector of interest, and total ray theoretic amplitudes can overcome limitations of the approximate equations. The application of the method is demonstrated in a synthetic case study and for real data acquired in the Campi Flegrei caldera, southern Italy.

The real data example is taken from the SERAPIS marine active seismic experiment (Section 4; Zollo *et al.* 2003). The main aims of this experiment were to image the detailed velocity structure within the caldera and adjacent regions (3-D first-arrival tomography), to map the caldera boundary in its submerged parts, to search for magma reservoirs, and to image the main subsurface discontinuities with reflected and mode-converted waves. Strong velocity contrasts are observed at some reflectors, and the available data set features variable source amplitudes and mainly wide-angle reflections. As mentioned above, standard AVO methods are typically applicable only to weak elastic contrasts and small incidence angles, and they require proper amplitude calibration. The need to overcome these limitations motivated the present study on *PS*-to-*PP* amplitude ratios. The Campi Flegrei case study presented here complements the 1-D interface model from deeper reflectors published in Zollo *et al.* (2008).

2 METHOD

A 1-D layered subsurface model is assumed, in which a constant interval *P*-velocity V_P , an interval *P*-to-*S* velocity ratio V_P/V_S and a density ρ is assigned to each layer (Fig. 1, top panel). Six parameters characterize a given reflector, that is, V_P , V_P/V_S and ρ above and below the reflector, corresponding to three parameter contrasts. The seismic sources and the receivers are located at the top of the model.

2.1 *PS*-to-*PP* amplitude ratios

Ignoring anelastic attenuation and anisotropy, the amplitudes A of primary *PP* and *PS* reflected phases at a given offset x depend on the source amplitudes S and receiver site effects X , on the geometrical spreading G , and on the reflection coefficients R at the reflector of interest

$$\begin{aligned} A_{PP}(x) &= S_{PP} \cdot X_{PP} \cdot G_{PP}(x) \cdot R_{PP}(x) \\ A_{PS}(x) &= S_{PS} \cdot X_{PS} \cdot G_{PS}(x) \cdot R_{PS}(x). \end{aligned} \quad (1)$$

The solid ray paths shown in Fig. 1 (bottom panel) for *PP* and *PS* reflections connect the same source and receiver. Considering the ratio $C(x)$ between the *PS* and *PP* amplitudes for this acquisition geometry, the effects of the source and the receiver site on the observed

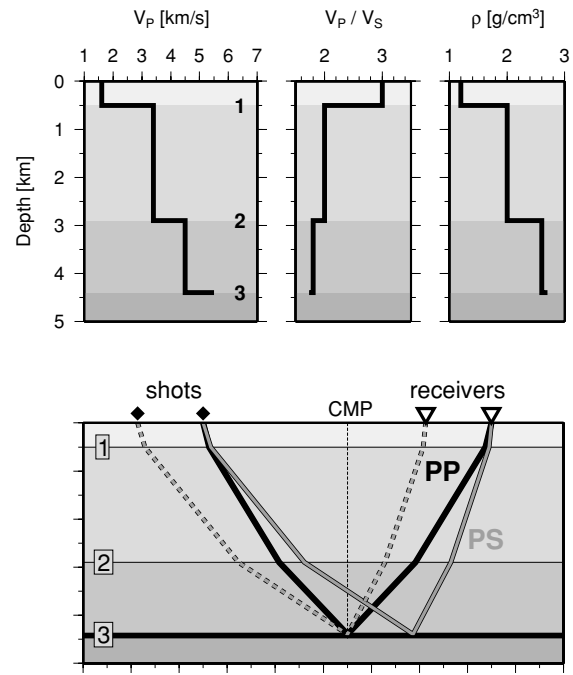


Figure 1. Top panels: layered 1-D model with constant *P*-velocity V_P , *P*-to-*S* velocity ratio V_P/V_S and density ρ in each layer. Bottom panel: sketch of ray paths for primary *PP* and *PS* reflections from interface 3. Whereas *PP* is reflected at the midpoint (CMP), the *PS* reflection point is located closer to the receiver. An additional, laterally shifted source–receiver pair can provide a *PS* observation for the same offset and reflection point as the *PP* reflection (dashed *PS* ray).

amplitudes are cancelled, because $S_{PP} = S_{PS}$ and $X_{PP} = X_{PS}$

$$\begin{aligned} C(x) &= \frac{A_{PS}}{A_{PP}}(x) \\ &= \frac{S_{PS}}{S_{PP}} \cdot \frac{X_{PS}}{X_{PP}} \cdot \frac{G_{PS}(x)}{G_{PP}(x)} \cdot \frac{R_{PS}(x)}{R_{PP}(x)} \\ &= \frac{G_{PS}(x)}{G_{PP}(x)} \cdot \frac{R_{PS}(x)}{R_{PP}(x)}. \end{aligned} \quad (2)$$

Eq. (2) and the related statement $S_{PP} = S_{PS}$ applies only for an isotropic point source such as an airgun shot or an explosion. In case of a vertical or horizontal point source the radiation pattern of the source has to be considered, because the take-off angles of the *PP*- and *PS*-reflected rays are different (Fig. 1; see also Kähler & Meissner 1983). The same applies to the receiver site where different incidence angles and polarizations of *PP*- and *PS*-waves have to be considered. Furthermore, amplitude partitioning onto the three sensor components depends on the seafloor or the free-surface elastic parameters (Wang *et al.* 2002). In the following we always assume an isotropic point source, and we use only three-component amplitudes (vector sums) to overcome the problem of amplitude partitioning.

Building the ratio of *PS* and *PP* amplitudes reduces also the effect of the geometrical spreading G , and the entire propagation effects in the overburden can be included by dynamic, ray theoretical forward modelling of the seismic amplitudes (Červený 2001). Thus, measured *PS*-to-*PP* amplitude ratios as a function of offset provide a means to estimate the elastic parameters at the reflector without the need for additional amplitude correction factors.

Whereas *PP* is reflected at the midpoint (CMP) between source and receiver, the corresponding *PS* reflection point lies closer to the receiver (Fig. 1, bottom panel). The asymmetry of the *PS* ray path

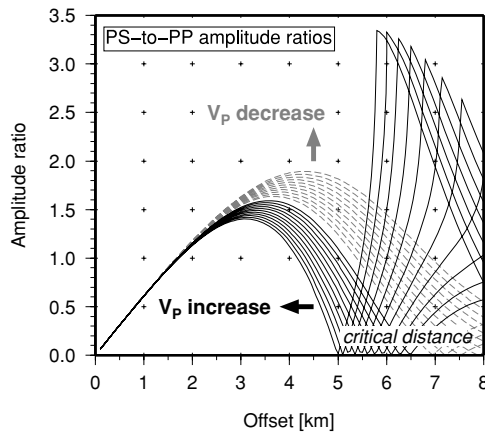


Figure 2. PS-to-PP amplitude ratios as a function of source–receiver offset for positive P -velocity contrasts (solid, black) and negative contrasts (grey, dashed) at interface 3 of the model shown in Fig. 1. Successive lines correspond to a 2 per cent increase or decrease relative to the P -velocity in the layer above the reflector (maximum variation $\Delta V_P = \pm 22$ per cent).

depends on the V_P/V_S ratios in the layers above the reflector. The distance between the CMP and the PS reflection point increases with increasing offset and decreasing reflector depth (Tessmer & Behle 1988). If the elastic parameter contrast at the reflector is varying laterally, the ratio between PS and PP reflected at the same subsurface location must be considered instead of the ratio calculated for the same source and receiver. An additional, laterally shifted source and receiver pair can provide the required PS observation (dashed PS ray path in Fig. 1). However, in this case the source amplitudes and possible receiver site effects have to be normalized before the calculation of the PS-to-PP ratios.

Fig. 2 shows example PS-to-PP amplitude ratio curves as a function of offset for interface 3 of the model shown in Fig. 1. These curves are calculated for a common offset of PS and PP. The black lines are for models with a positive P -velocity contrast at that interface (increasing V_P with depth), and the grey curves are related to models with a negative contrast (decreasing V_P). The amplitude ratio variation with offset is dominated by the amplitude behaviour of the PS reflection. At zero offset the PS-to-PP ratio vanishes, and the influence of the elastic parameter contrast on the PS-to-PP amplitude ratios increases towards intermediate offsets (see also Zhang & Mancini 2006). For a positive V_P contrast, the amplitude ratio curves approach zero again at the distance of critical P-to-S reflection, followed by a rapid increase at post-critical distances. If this is observed, the trade-off between V_P and density (seismic impedance) may be resolved, because the critical distance depends only on the V_P contrast. In case of a negative V_P contrast a critical reflection does not exist, resulting in smooth amplitude ratio curves with one single peak.

The possibilities and limitations of PS-to-PP amplitude ratio analyses are demonstrated in synthetic examples with the model shown in Fig. 1 and with different ranges of source–receiver offset. In one example, we introduce a positive P -velocity contrast of $\Delta V_P = 22$ per cent at interface 3 and for another one a negative contrast of $\Delta V_P = -22$ per cent at the same interface. The corresponding PS-to-PP amplitude ratio curves are included in Fig. 2. The potential results of some assumed PS-to-PP amplitude ratio analyses can be presented as slices through the model parameter space showing the least-squares misfit L between measured and computed ratios as a function of two model parameters. For N off-

sets the misfit function is defined as

$$L = \sqrt{\frac{1}{N} \sum_{i=1}^N (C_i^{\text{obs}} - C_i^{\text{cal}})^2} \quad (3)$$

in which C_i^{obs} and C_i^{cal} denote the measured and computed amplitude ratios at one offset x_i , respectively (eq. 2).

Each group of three panels in Fig. 3 shows such slices through the parameter space for the three model parameters below the reflector, for example, V_P versus V_P/V_S (top left-hand panels). Figs 3(a)–(c) illustrate the case of a positive velocity contrast at the reflector. Considering an acquisition geometry with a maximum offset of 4 km (Fig. 3a), only pre-critical PS-to-PP amplitude ratios are evaluated (see Fig. 2). The small variation of the short-offset PS-to-PP curves with a variation of the subreflector model parameters leads to small misfits L for a relatively wide range of model parameters, that is, ambiguous results. The dominant ambiguity is visible in the plot of V_P versus ρ below the reflector (dark region in the bottom left-hand panel of Fig. 3a). An increase of the maximum offset to 6 km (Fig. 3b) includes the characteristic zero-crossing of the PS-to-PP curve at the critical distance of 5 km. Since this feature of the PS-to-PP curve well constrains V_P below the reflector, also V_P/V_S and ρ are significantly better resolved than with the short-offset data, as indicated by smaller dark regions in the misfit plots. A maximum offset of 8 km further improves the resolution, especially of the density ρ (Fig. 3c). In case of a negative V_P contrast at the reflector large offsets are required to retrieve reasonable estimates of the model parameters below the reflector (Fig. 3d). The pronounced trade-off between V_P and ρ cannot be resolved here. For example, a model with a lower V_P but a higher ρ below the reflector would fit the observed PS-to-PP ratios similarly well as the true model.

As a final example, Fig. 4 illustrates that the six model parameters V_P , V_P/V_S and ρ above and below a certain reflector are not independent. Again three panels show slices through the model parameter space at interface 3, this time always for two corresponding model parameters above and below the reflector (e.g. $V_{P,1}$ above versus $V_{P,2}$ below). The remaining four parameters are kept constant at the values of the true reference model (see Fig. 1). Generally, a higher V_P in the layer above the reflector leads to a higher V_P estimate in the layer below (left-hand panel) and vice versa. A similar behaviour can be seen for V_P/V_S and the density ρ , that is, the PS-to-PP amplitude ratio variation with offset mainly provides estimates on parameter contrasts at a reflector. Therefore, some of the parameters must be constrained before an inversion.

2.2 Estimation of elastic parameters

Basic PP reflection processing includes common-midpoint gathering of vertical-component traces, static corrections, filtering, normal-moveout (NMO) velocity analysis, NMO correction and stacking (e.g. Yilmaz 2001). A modified processing sequence is necessary for PS waves. The radial-component traces are typically sorted into common-conversion point gathers, and the velocity analysis searches for an effective P-to-S velocity ratio suitable for the converted-wave NMO correction of an individual PS reflection (Audebert *et al.* 1999; Thomsen 1999; Li & Yuan 2003). Some iterations of trace gathering and effective velocity analysis may be required in case of lateral variations, because the conversion point depends on the chosen velocity ratio. The obtained PP NMO velocities and the effective velocity ratios for PS can be converted into an interval velocity model as a function of depth (see e.g. Yilmaz 2001; Tessmer & Behle 1988, respectively). If PP and PS traveltimes picks

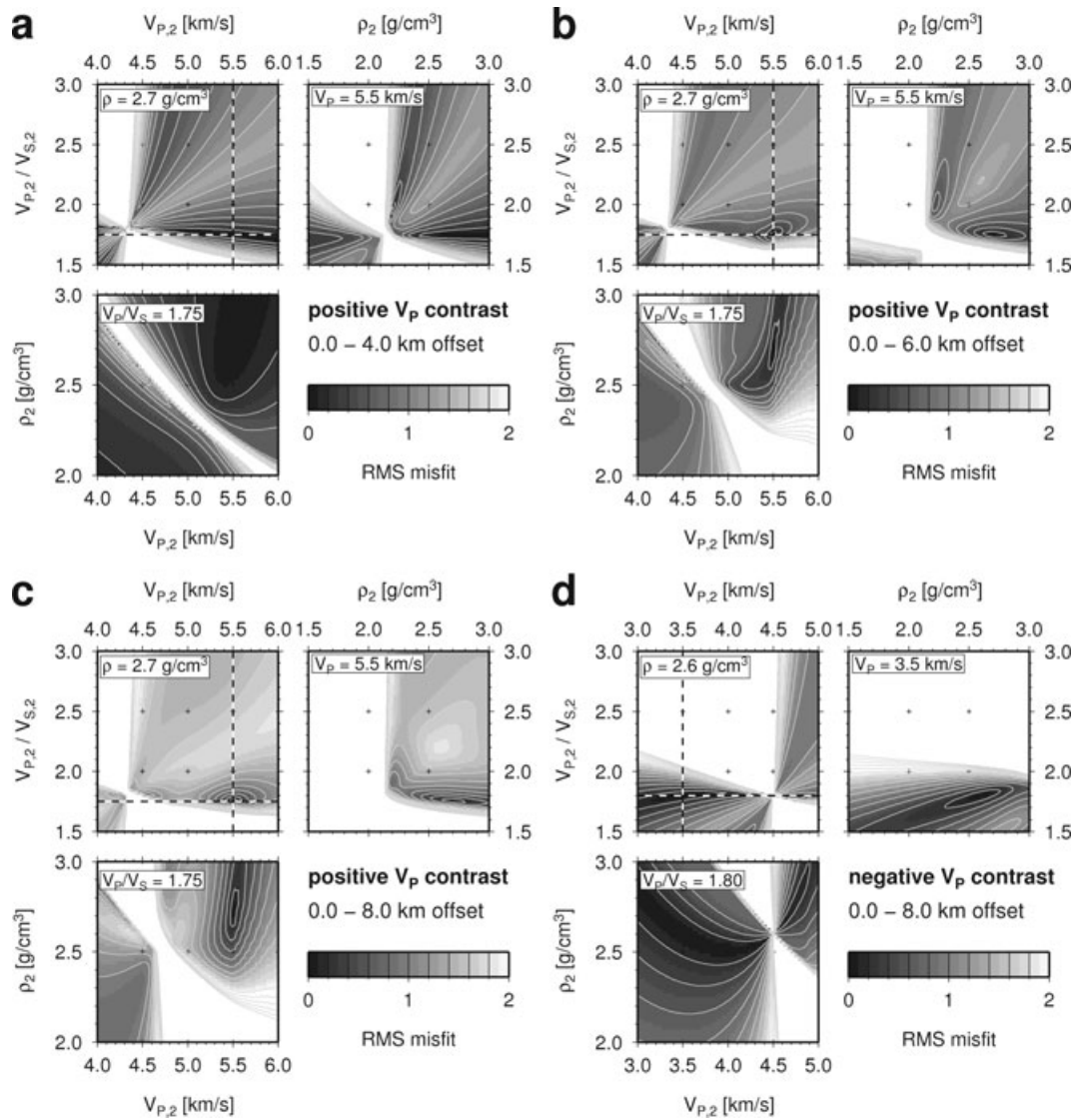


Figure 3. Slices through the model parameter space showing the colour-coded misfit L (eq. 3) between measured and computed amplitude ratios as a function of two model parameters below interface 3 (see Fig. 1). The remaining third parameter below the interface is fixed to the true value of the model. Panels (a–c): rms misfit for a model with a P -velocity increase from 4.5 to 5.5 km s⁻¹ ($\Delta V_P = 22$ per cent) and three different source–receiver offset ranges. Panel (d): rms misfit for a P -velocity decrease to 3.5 km s⁻¹ ($\Delta V_P = -22$ per cent).

are available, also ray tracing can provide the interval velocity model.

Our aim is to estimate the elastic contrasts at selected reflectors that have been identified in the (processed) seismic data. In a first step, we pick the PP traveltimes of the target reflector on unstacked, vertical-component seismograms and the corresponding PS traveltimes on the radial-component sections. The second step is the measurement of PP and PS amplitudes in a time window including the entire reflection wavelet. Especially for wide-angle seismic data the PP and PS amplitudes cannot be simply extracted from the vertical and horizontal components, respectively, because, as mentioned above, the amplitude partitioning onto these two components depends on the seafloor or free-surface elastic parameters (Wang *et al.* 2002; Wang & Singh 2003). Therefore, we extract the complete three-component amplitudes (vector sums) for both the PP and the PS reflections. This approach also avoids any error related to possible uncertainties in the orientations of the three-component sensors.

Once the three-component PP and PS amplitudes of the selected target reflector are measured at all offsets, the PS -to- PP ratios at common offsets are calculated and the elastic parameter contrast can be estimated. We constrain the velocity structure above the reflecting interface using a layered interface velocity model from traveltime modelling or obtained during the data processing as mentioned above. Additionally we assign initial values for the densities, for example, using an empirical velocity–density relation (e.g. Gardner *et al.* 1974). Then we calculate theoretical PS -to- PP amplitude ratios at common offsets of PP and PS using dynamic ray tracing in the layered model (Farra & Madariaga 1987). Finally, we vary the unconstrained model parameters (V_P , V_P/V_S , ρ below the reflector) to minimize the misfit L between observed and theoretical amplitude ratio curves (eq. 3). The minimization process is a grid search through the model parameter space, possibly combined with Simplex optimization to find a local minimum (e.g. Press *et al.* 1992). Slices through the parameter space showing the misfit value as a function of selected model parameters provide an estimate of

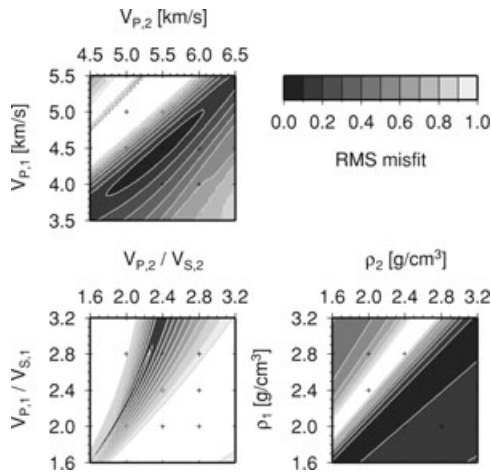


Figure 4. Slices through the model parameter space showing the colour-coded misfit L (eq. 3) between measured and computed amplitude ratios of two model parameters at interface 3 (see Fig. 1). The remaining four parameters are kept constant at the values of the reference model. Index 1 denotes the parameter above the reflector and index 2 the corresponding one below.

the uncertainty of the solution. An entire layered subsurface model can be constructed by a layer stripping procedure, beginning with the shallowest reflector of interest.

3 SYNTHETIC CASE STUDY

A dipping reflector and a laterally varying overburden violates the assumption of a 1-D model. To illustrate these effects on the analysis of *PS-to-PP* amplitude ratios, we apply the method to amplitude ratios extracted from synthetic data for a hypothetical volcanic caldera structure (Fig. 5). The target of this case study is a segment of the deepest reflector in the 2-D model. The subsurface structure above the target shows some lateral variation, and the target reflector itself is dipping towards the left-hand side of the profile (Fig. 5, top panel). The data to be analysed are three-component seismograms generated for a line of shots in a shallow water layer and recorded at a single multicomponent receiver at the sea bottom. These data were computed with the dynamic ray modelling tool NORSAR-2D (NORSAR 2003). Primary *PP* and *PS* reflections from all model interfaces are included in the vertical- and radial-component synthetic seismograms shown in Fig. 6. The transverse component is zero in this case.

First, we use ray tracing to construct an approximate 1-D interval velocity model from the *PP* and *PS* reflection traveltimes of the target reflector and of the three reflectors above (Fig. 5, bottom panel). The densities for each layer above the target reflector are taken from the 2-D model. Second, we measure the *PP* and *PS* amplitudes for the target reflector in a 0.15 s time window from the three-component seismograms, excluding those parts of the reflection signals that are obviously contaminated by other phases. Third, theoretical *PS-to-PP* amplitude ratios for this model are fit to the measured curve by varying V_P , V_P/V_S and the density ρ in the layer below the reflector. Here, the *PS-to-PP* amplitude ratio curve is an average of that for negative offsets and that for positive offsets.

Fig. 7 is an overlay plot of the measured amplitude ratios (dots, diamonds) and a theoretical curve for the best-fitting model obtained with the density contrast fixed to the known value (thick grey line). The additional solid black and dashed grey curves are for alternative models with 10 per cent higher and 10 per cent lower

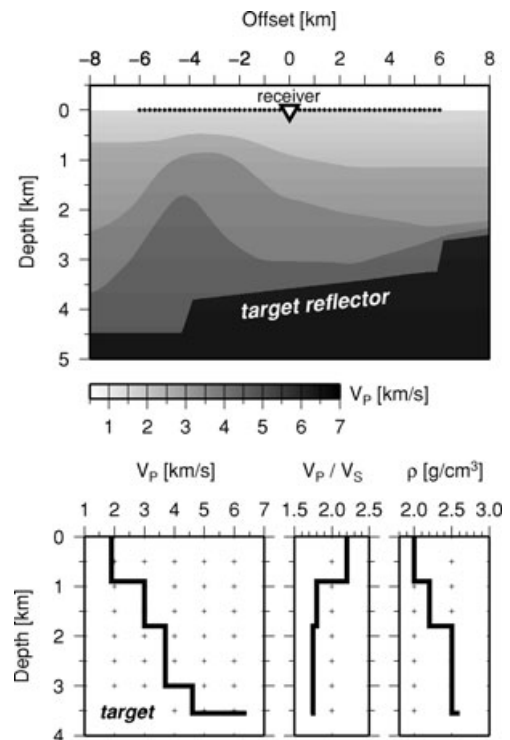


Figure 5. Top panel: 2-D P -velocity model used in the synthetic case study, and shots (dots) and a receiver (triangle) of a common receiver gather. Bottom panel: approximate 1-D model based on traveltimes for the common receiver gather. The V_P/V_S ratios and densities are the same as in the 2-D model.

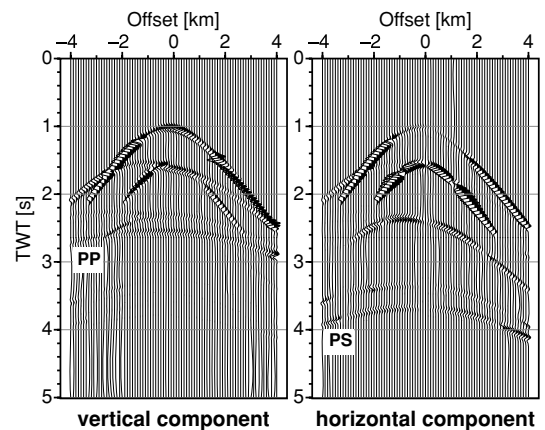


Figure 6. Synthetic vertical- and horizontal-component seismograms for all primary *PP* and *PS* reflections of the common receiver gather shown in Fig. 5 (top panel). The target reflections are labelled *PP* and *PS*.

V_P contrasts, respectively. The critical distance for the estimated (and true) P -velocity contrast is reached at an offset of about 3 km. Measured pre-critical amplitude ratios (black dots) are fit well by the theoretical values. For the positive offset branch the measured *PS-to-PP* amplitude ratios approach zero at a smaller offset than the theoretical curve, which suggests a higher V_P contrast than that of the best 1-D average model. The opposite observation is made for the negative offset branch, demonstrating that this is related to the reflector dip. Post-critical amplitude ratios (grey diamonds) are much more sensitive to small changes of elastic parameters and incidence angles. Measured post-critical amplitude ratios do not match the theoretical values for the approximate 1-D model, also because

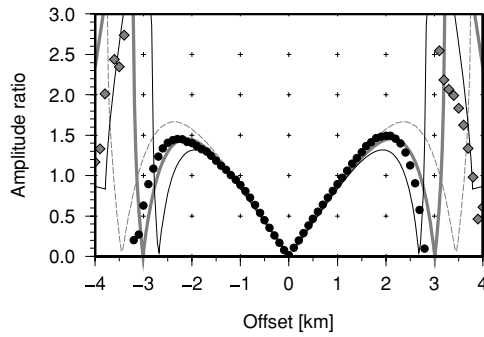


Figure 7. Synthetic *PS*-to-*PP* amplitude ratio curves overlain with pre-critical (black dots) and post-critical (grey diamonds) amplitude ratios. The thick grey line is the theoretical curve for the 1-D model shown in Fig. 5, and thin lines correspond to models with 10 per cent higher and lower *P*-velocity in the layer below the target reflector.

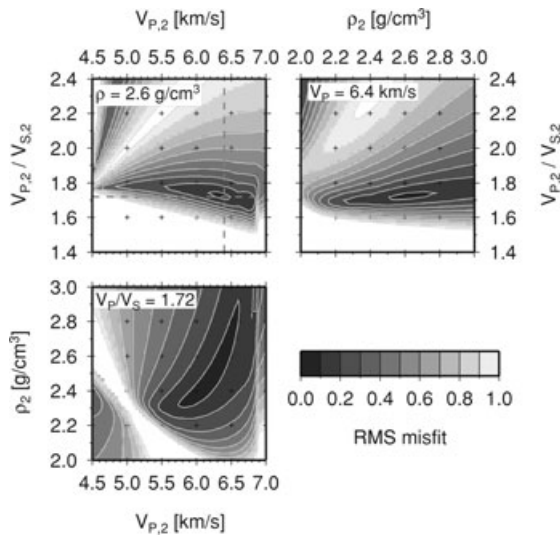


Figure 8. Slices through the parameter space for the model parameters in the layer below the target reflector. The 1-D velocity and density structure above the target is shown in Fig. 5.

of the reflector dip and because of the lateral velocity variation in the overburden.

Fig. 8 illustrates the resolution of the estimated elastic parameters below the target reflector. Each of the three panels shows the misfit *L* between the measured pre-critical *PS*-to-*PP* amplitude ratios and the theoretical values as a function of two elastic parameters for the layer below the reflector. The third parameter for the layer below and the three parameters of the layer above are kept constant at the value of the best 1-D model (Fig. 5, bottom panel). The dark regions in these slices through the model parameter space outline elastic parameter combinations that yield a good fit, that is, a narrow dark region indicates a better resolution of the related parameter than a wide region of possible values. In the panel for *V_p* and density ρ (bottom left-hand panel) the trade-off between these two parameters is clearly visible as a large region of probable *V_p*- ρ pairs. A similar but less pronounced parameter correlation can be seen in the other two panels (*V_p*/*V_s* versus *V_p* and ρ versus *V_p*/*V_s*). An uncertainty of 10–15 per cent for each estimated elastic parameter may be assigned here.

4 APPLICATION TO REAL DATA

The reflection seismic data for this case study came from the SERAPIS marine active seismic experiment carried out in the eastern Tyrrhenian Sea near the coast of southern Italy (e.g. Zollo *et al.* 2003). During this experiment a large number of airgun shots was recorded by a grid of 30 three-component ocean bottom seismometers (OBS) in the Bay of Pozzuoli, which covers parts of the Campi Flegrei volcanic caldera (Fig. 9). This caldera was formed mostly by two large explosive events (Orsi *et al.* 1996) about 37–39 ka (Campanian Ignimbrite) and about 12–15 ka ago (Neapolitan Yellow Tuff). The current activity of the caldera is demonstrated by hydrothermal activity, gas emissions, and large-scale vertical ground movements. The most recent uplift episodes in 1970–1972 and 1982–1984 lead to a cumulative uplift of 3.5 m and were accompanied by a series of earthquake swarms. Details and further references on the geological setting of the caldera can be found in Orsi *et al.* (1996), Zollo *et al.* (2003) and Dello Iacono *et al.* (2009), among others.

The average water depths at the OBS locations in the Bay of Pozzuoli is about 100 m, and the orientations of their two horizontal components have been determined by polarization analysis of the direct wave travelling in the water layer. The three-component recordings were initially arranged into common-midpoint (CMP) gathers (500 × 500 m cells), which contain more than 120 traces each in the central part of the bay (Dello Iacono *et al.* 2009). Besides rotation of the two horizontal components into the radial and transverse direction, the data processing included 5–15 Hz bandpass filtering for the amplitude analyses and additional trace amplitude normalization for phase identification.

In a previous study of Dello Iacono *et al.* (2009), strong *PP* and *PS* reflections have been identified for a shallow reflector beneath the Campi Flegrei caldera, and the *PS* reflections have been used to determine an average *V_p*/*V_s* ratio of 3.6 for the layer above the reflector. As an example, Fig. 10 shows vertical- and radial-component

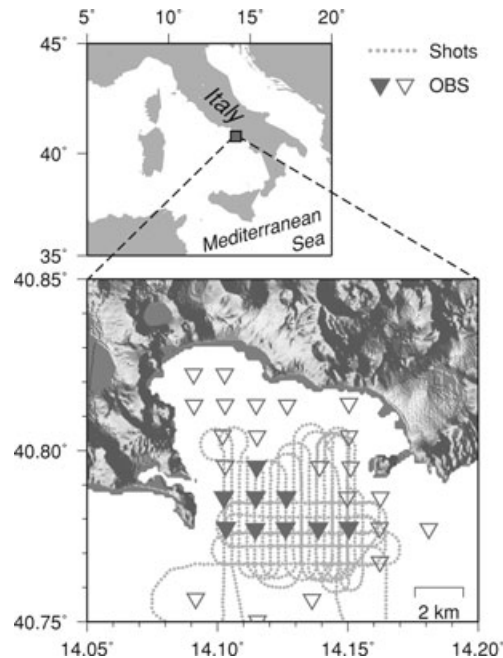


Figure 9. Location of the study area in the Bay of Pozzuoli, southern Italy, and the seismic acquisition geometry. Dots indicate airgun shots and inverted triangles three-component ocean bottom seismometers (OBS) of the SERAPIS experiment (filled symbols: OBS used in this study).

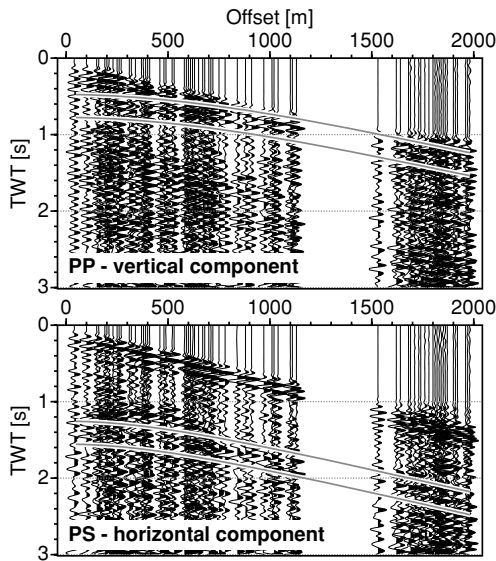


Figure 10. Example of vertical- and horizontal-component seismicograms. The traces are sorted by source–receiver distance, 5–15 Hz bandpass-filtered, and amplitude-normalized. The grey lines mark time windows around the theoretical *PP* and *PS* arrival times, respectively.

seismograms taken from one CMP gather of the SERAPIS data set. The lines mark time windows around the theoretical *PP* and *PS* arrival times, calculated for a reflector depth of 0.6 km and the velocity model given below. In this study, we manually picked traveltimes of the *PP* and *PS* reflections from all analysed sections (Fig. 11, top panel). Then we used these picks to extract the three-component seismic amplitudes in a 0.2 s time window for a subsequent *PS*-to-*PP* amplitude ratio analysis. A maximum source–receiver offset of 2 km is considered here.

The aim is to obtain the average velocities below the subhorizontal, flat reflector and to estimate the density contrast from a single average *PS*-to-*PP* amplitude ratio curve derived from all measured ratios. Fig. 11 (bottom panel) shows the amplitude ratio curve as a function of offset, wherein each dot represents the mean of the measured ratios within a 100 m wide offset bin. The maximum amplitude ratio is observed at 0.45 km offset, within a region of rather large variability (offset range 0.3–0.8 km). In the far offset range, the *PS*-to-*PP* amplitude ratios decrease continuously with increasing offset.

The shallow 3-D *P*-velocity structure above the target reflector is known from 3-D high-resolution tomography studies using first-arrival traveltimes from the SERAPIS data set (Zollo *et al.* 2003; Dello Iacono *et al.* 2009). From these models we extracted a local 1-D average *P*-velocity model for the region covered by our reflection data. This 1-D model served as a starting model to estimate the velocities above the reflector and the reflector depth by 1-D kinematic ray tracing of *PP* and *PS* reflections. Based on several trial-and-error runs of the ray tracing procedure to fit observed and modelled *PP* and *PS* traveltimes, we fixed the depth of the target reflector at 0.6 km and constrained the velocities above the reflector. In this 1-D model, the *P*-velocity increases linearly from $V_{P,1} = 1.55 \text{ km s}^{-1}$ at the seafloor to $V_{P,1} = 1.95 \text{ km s}^{-1}$ directly above the reflector, and the average vertical *P*-to-*S* velocity ratio is $V_{P,1}/V_{S,1} = 3.6$. In addition we assigned a density of $\rho_1 = 2.2 \text{ g cm}^{-3}$. Based on this model for the shallow layer, the shape of the observed *PS*-to-*PP* amplitude ratio curve can be modelled by positive *P*- and *S*-velocity contrasts with $V_{P,2} = 3.5 \text{ km s}^{-1}$ and

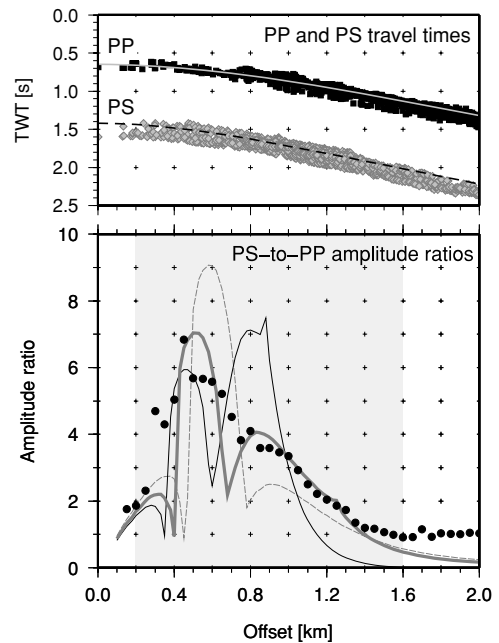


Figure 11. Top panel: measured *PP* and *PS* traveltimes as a function of offset, overlain by theoretical times (lines) for the model given below. Bottom panel: measured (dots) and modelled (thick grey line) *PS*-to-*PP* amplitude ratios versus offset. The model parameters are $V_{P,1} = 1.55\text{--}1.95 \text{ km s}^{-1}$, $V_{P,1}/V_{S,1} = 3.6$ and $\rho_1 = 2.2 \text{ g cm}^{-3}$ above the reflector at 0.6 km depth, and $V_{P,2} = 3.5 \text{ km s}^{-1}$, $V_{P,2}/V_{S,2} = 1.75$ and $\rho_2 = 2.3 \text{ g cm}^{-3}$ below. The thin lines are theoretical curves for a model with 10 per cent higher $V_{P,2}$ (solid) and 10 per cent lower $V_{P,2}$ (dashed). The grey-shaded area outlines the offset range used to generate the panels Fig. 12.

$V_{P,2}/V_{S,2} = 1.75$ in the half-space below the reflector (thick grey line in Fig. 11, bottom panel).

For this strong contrast, the distance related to the critical *P*-to-*P* reflection is reached near 0.7 km offset, and the corresponding *P*-to-*S* reflection with the same incident angle arrives at 0.4 km offset. This can explain the larger variability of the observed *PS*-to-*PP* amplitude ratios in this offset range, because even small velocity variations have a great influence on the critical reflection points and the peaks of the corresponding *PS*-to-*PP* amplitude ratio curves (thin lines in Fig. 11, bottom panel).

Slices through the model parameter space illustrate the resolution of the obtained model given above (Fig. 12a). Each panel shows the misfit between observed and modelled *PS*-to-*PP* amplitude ratios as a function of two model parameters below the reflector, while fixing the third parameter and the values above the reflector. Only the offset range from 0.2 to 1.6 km is considered here (shaded area in Fig. 11), because the small *PS*-to-*PP* ratios at very short and at large offsets may be biased by noise in the data. The minima of the misfit function L are narrow, suggesting good estimates of the model parameters in the half-space below the reflector. The best fit is obtained for $V_{P,2} = 3.5 \text{ km s}^{-1}$, $V_{P,2}/V_{S,2} = 1.75$ and $\rho_2 = 2.3 \text{ g cm}^{-3}$, in which the density ρ_2 shows the greatest uncertainty. For comparison, Fig. 12(b) shows the same slices through the parameter space, but computed for *PS*-to-*PP* ratios from noise-free synthetic seismograms for the best-fitting model. The similarity of the results for real and synthetic data supports our model with the assumption of a flat reflector and of lateral homogeneity.

The shallow layer and its high *P*-to-*S* velocity ratio of $V_{P,1}/V_{S,1} = 3.6$ can be related to incoherent, water-saturated volcanic and marine sediments, corroborated also by rock physics

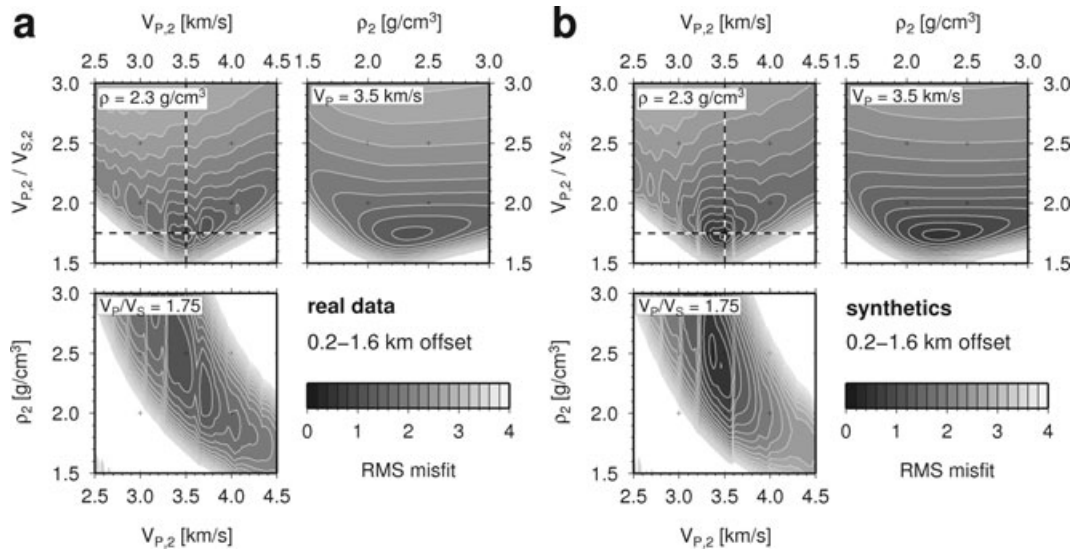


Figure 12. Slices through the parameter space for the model parameters in the half-space below the reflector at 0.6 km depth. Velocities and density in the layer above the reflector are given in the caption of Fig. 11. (a) Misfit function L (eq. 3) calculated for the real data in the offset range 0.2–1.6 km and (b) misfit function for noise-free synthetics from the best-fitting model instead of real data.

modelling (Dello Iacono *et al.* 2009). The P -velocity of about $V_{P,2} = 3.5 \text{ km s}^{-1}$ is consistent with results from previous studies (e.g. Zollo *et al.* 2003; Zollo *et al.* 2008), and the reflector at 0.6 km depth may be related to tuffs, most likely interbedded with solidified lavas (e.g. Bruno 2004). In a recent paper, Zollo *et al.* (2008) show additional results of PS -to- PP amplitude ratio analyses for two deeper reflectors in the same study area (2.7 km and a magma layer at 7.5 km depth), focusing on the results and their volcanological implications.

5 DISCUSSION

We introduced a method to estimate seismic velocity and density contrasts at nearly flat reflectors in a 1-D layered model using PS -to- PP amplitude ratios as a function of source–receiver offset. As for all AVO or AVA methods using PP and PS simultaneously, these two phases must be preliminarily identified for the same reflector (event correlation), which can be a challenging task with real data. The most reliable association of these two phases can be made from well log data. If such data are not available, one may rely on PP and PS reflection moveout analysis on vertical- and radial-component seismograms, possibly guided by kinematic ray tracing. For short-offset data a natural separation of PP energy on the vertical and PS energy on the horizontal component sections can be observed in regions with a shallow low-velocity layer causing near-vertical ray paths near the surface. A complete separation of the P - and S -wavefields from wide-angle multicomponent data is possible in the time–slowness (τ – p) domain (Wang *et al.* 2002; Wang & Singh 2003), and the receiver function method (Edme & Singh 2008) may help to identify the PS arrivals.

Once the PP and PS phases are identified and their traveltimes are picked, the PS -to- PP amplitude ratio analysis yields elastic parameter contrasts at reflectors using wide-angle reflection data, and the method does not require additional amplitude correction factors as needed for standard AVO techniques. However, at small offsets the PS -to- PP amplitude ratios do not change significantly with the V_P contrast at the reflector. Additionally, noise in real

data has a stronger influence on the small PS amplitudes at short offsets and may introduce a systematic bias towards higher PS -to- PP amplitude ratios. Therefore, amplitude ratio measurements are needed for sufficiently large offsets. If this is the case, the method is applicable also to subsurface structures that violate the 1-D assumption by a slightly dipping reflector or a laterally varying overburden, as demonstrated in the synthetic case study using pre-critical amplitude ratios. If the distance of critical reflection is detected in the PS -to- PP ratio curve, the associated positive V_P contrast is well-resolved, and also a good estimate for V_P/V_S can be expected. The recovery of density contrasts from pre-critical amplitude ratios requires additional constraints, for example, from empirical velocity–density relations or gravity data. If no significant lateral variation of the subsurface structure is observed, post-critical amplitude ratios may be included in the analysis, which can also improve the resolution of density contrasts (see also Downton & Ursenbach 2006).

In several cases such as gas sands the P -wave amplitudes go to zero before changing the polarity (e.g. Li *et al.* 2006). Hence this will introduce a singularity in the PS -to- PP amplitude ratio curves. While this behaviour may be considered as a strong point in our analysis method, an automatic inversion procedure does not permit any singularity. Therefore, only PP amplitudes above a certain threshold should be used to calculate the ratios.

Another important issue in our method is the requirement of an accurate velocity model to compute the ray paths above the target reflector, that is, errors in the velocity model above the reflector affect the obtained model parameters below the reflector (or the parameter contrasts). Changes of the velocities in the hanging wall lead to changes of the incidence angles at the reflector and of the location of the PS reflection point. For example, incidence angles would be underestimated, if a layered model with a positive velocity gradient in the hanging wall is replaced by a single layer with average velocities. This is a general weakness of AVO methods as opposed to AVA analyses. One way to address this problem could be to transform the data in the τ – p domain and analyse PS -to- PP ratios as a function of slowness instead of offset (Edme & Singh 2008). This approach would require densely spaced profiles, and not both

the source and the receiver effects are cancelled as in the method presented here.

The real data example from the Campi Flegrei caldera features strong P - and S -velocity contrasts at a shallow reflector (0.6 km), and the distance of critical reflection is therefore reached already at short offsets. The obtained model is based mostly on post-critical PS -to- PP amplitude ratios, which are more sensitive to violations of the 1-D assumption of our method than the pre-critical ratios. However, old 2-D near-vertical seismic reflection profiles (Finetti & Morelli 1974) across our study region show flat, subhorizontal sedimentary layers without an indication for significant lateral velocity variations above our target reflector (Lines NA-4 and NA-5 in Bruno 2004). Additionally, the target reflector itself shows only minor topography within our small study region. Therefore, the assumption of a 1-D subsurface structure is justified here.

The P -velocities obtained from seismic reflection analysis are consistent with a high-resolution tomographic model for the Campi Flegrei caldera (Zollo *et al.* 2003), and a similar high V_P/V_S ratio in the very shallow subsurface has been reported in Dello Iacono *et al.* (2009). Aster & Meyer (1988) derived a tomographic model for V_P and V_S beneath the caldera using earthquake data from the uplift episode in the early 1980s. For our study region, which is located near the southern boundary of their model, they found values of $V_P = 2.8 \text{ km s}^{-1}$ and $V_P/V_S = 1.7$. The deviation from our model may be explained by the fact that a tomographic inversion tends to smooth sharp velocity contrasts. The value of V_P/V_S is well in agreement with our results for the layer below the reflector at 0.6 km depth. The high V_P/V_S ratios of the shallow marine sediments could not be resolved by Aster & Meyer (1988) because of the use of earthquakes and onshore stations only.

6 CONCLUSIONS

The PS -to- PP amplitude ratio analysis can be recommended for wide-angle seismic reflection data, especially when strong, positive elastic parameter contrasts are expected and when source amplitudes or site effects are poorly known. The application of our method to a 0.6 km deep reflector beneath the Campi Flegrei caldera revealed a strong V_P increase from nearly 2 to 3.5 km s^{-1} , a V_P/V_S decrease from 3.6 to 1.75, and a small density contrast of $\Delta\rho = 0.1 \text{ g cm}^{-3}$. The reflector marks the boundary between solid volcanic rocks (tuffs/lavas) below and unconsolidated marine and volcanic sediments above.

ACKNOWLEDGMENTS

We thank three anonymous reviewers for their constructive comments and suggestions. 1-D forward ray modelling was done with the dynamic ray tracer RAYINTPL2PT written by Véronique Farra, and we used Seismic Unix (Cohen & Stockwell 2007) for data processing and the Generic Mapping Tools (GMT) to generate the figures. This study has been carried out with financial support from the Italian Department of Civil Protection and INGV in the research framework program V4 (2006–2007).

REFERENCES

Aki, K. & Richards, P.G., 2002. *Quantitative Seismology*, 2nd edn, University Science Books, Sausalito, CA.
 Aster, R.C. & Meyer, R.P., 1988. Three-dimensional velocity structure and hypocenter distribution in the Campi Flegrei caldera, Italy, *Tectonophysics*, **149**(3–4), 195–218, doi:10.1016/0040-1951(88)90173-4.

Audebert, F., Granger, P.Y. & Herrenschildt, A., 1999. CCP-scan technique (1): true common conversion point sorting and converted wave velocity analysis solved by PP and PS pre-stack depth migration, *SEG Expanded Abstracts*, **18**, 1186–1189, doi:10.1190/1.1820716.
 Auger, E., Virieux, J. & Zollo, A., 2003. Locating and quantifying the seismic discontinuities in a complex medium through the migration and AVA analysis of reflected and converted waves: an application to the Mt. Vesuvius volcano, *Geophys. J. Int.*, **152**(2), 486–496, doi:10.1046/j.1365-246X.2003.01864.x.
 Avseth, P., Mukerji, T. & Mavko, G., 2005. *Quantitative Seismic Interpretation: Applying Rock Physics Tools to Reduce Interpretation Risk*, Cambridge University Press, Cambridge, UK.
 Bruno, P.P., 2004. Structure and evolution of the Bay of Pozzuoli (Italy) using marine seismic reflection data: implications for collapse of the Campi Flegrei caldera, *Bull. Volc.*, **66**, 342–355, doi:10.1007/s00445-003-0315-9.
 Castagna, J.P. & Smith, S.W., 1994. Comparison of AVO indicators: a modeling study, *Geophysics*, **59**(12), 1849–1855, doi:10.1190/1.1443572.
 Červený, V., 2001. *Seismic Ray Theory*, Cambridge University Press, Cambridge.
 Cohen, J.K. & Stockwell, J.W., 2007. CWP/SU: Seismic Unix Release 40: an open source software package for seismic research and processing, Center for Wave Phenomena, Colorado School of Mines, Golden, Colorado. <http://www.cwp.mines.edu/cwpcodes/>.
 Dello Iacono, D., Zollo, A., Vassallo, M., Vanorio, T. & Judenherc, S., 2009. Seismic images and rock properties of the very shallow structure of Campi Flegrei caldera (southern Italy), *Bull. Volc.*, **71**(3), 275–284, doi:10.1007/s00445-008-0222-1.
 Downton, J.E. & Ursenbach, C., 2006. Linearized amplitude variation with offset (AVO) inversion with supercritical angles, *Geophysics*, **71**(5), E49–E55, doi:10.1190/1.2227617.
 Edme, P. & Singh, S.C., 2008. Receiver function method in reflection seismology, *Geophys. Prospect.*, **56**(3), 327–340, doi:10.1111/j.1365-2478.2007.00685.x.
 Farra, V. & Madariaga, R., 1987. Seismic waveform modeling in heterogeneous media by ray perturbation theory, *J. geophys. Res.*, **92**(B3), 2607–2712, doi:10.1029/JB092iB03p02697.
 Finetti, I. & Morelli, C., 1974. Esplorazione sismica a riflessione dei Golfi di Napoli e Pozzuoli, *Bollettino di Geofisica Teorica ed Applicata*, **16**(62–63), 175–222.
 Gardner, G.H.F., Gardner, L.W. & Gregory, A.R., 1974. Formation velocity and density—the diagnostic basics for stratigraphic traps, *Geophysics*, **39**(6), 770–780, doi:10.1190/1.1440465.
 Hilterman, F.J., 2001. Seismic amplitude interpretation, Number 4 in Distinguished Instructor Series. Society of Exploration Geophysicists, and European Association of Geoscientists and Engineers.
 Ibrahim, A.-B.K., 1971. The amplitude ratio PcP/P and the core-mantle boundary, *Pure appl. Geophys.*, **91**(1), 114–133, doi:10.1007/BF00879561.
 Iidaka, T., Takeda, T., Kurashimo, E., Kawamura, T., Kaneda, Y. & Iwasaki, T., 2004. Configuration of subducting Philippine Sea plate and crustal structure in the central Japan region, *Tectonophysics*, **388**(1–4), 7–20, doi:10.1016/j.tecto.2004.07.002.
 Kähler, S. & Meissner, R., 1983. Radiation and receiver pattern of shear and compressional waves as a function of Poisson's ratio, *Geophys. Prospect.*, **31**(3), 421–435, doi:10.1111/j.1365-2478.1983.tb01061.x.
 Kurt, H., 2007. Joint inversion of AVA data for elastic parameters by bootstrapping, *Comp. Geosci.*, **33**(3), 367–382, doi:10.1016/j.cageo.2006.08.012.
 Li, X.-Y. & Yuan, J., 2003. Converted-wave moveout and conversion-point equations in layered VTI media: theory and applications, *J. appl. Geophys.*, **54**, 979–318, doi:10.1016/j.jappgeo.2003.02.001.
 Li, X.Y., Chen, S., Sun, X., Pei, J. & Dai, H., 2006. Multicomponent PP and PS seismic response from volcanic gas reservoirs, in *68th EAGE Conference and Exhibition*, Vienna, Austria, European Association of Geoscientists and Engineers. A005.
 Margrave, G.F., Stewart, R.R. & Larsen, J.A., 2001. Joint PP and PS seismic inversion, *Leading Edge*, **20**(9), 1048–1052, doi:10.1190/1.1487311.

- Meissner, R. & Hegazy, M.A., 1981. The ratio of the PP to the SS-reflection coefficient as a possible future method to estimate oil and gas reservoirs, *Geophys. Prospect.*, **29**(4), 533–540, doi:10.1111/j.1365-2478.1981.tb00693.x.
- NORSAR, 2003. *NORSAR-2D Ray Modelling version 5.0 — User's Guide*, NORSAR Innovation AS, P.O. Box 53, 2027 Kjeller, Norway, <http://www.norsar.com>.
- Orsi, G., De Vita, S. & di Vito, M., 1996. The restless, resurgent Campi Flegrei nested caldera (Italy): constraints on its evolution and configuration, *J. Volc. Geotherm. Res.*, **74**(3–4), 179–214, doi:10.1016/S0377-0273(96)00063-7.
- Ostrander, W.J., 1984. Plane-wave reflection coefficients for gas sands at nonnormal angles of incidence, *Geophysics*, **49**(10), 1637–1648, doi:10.1190/1.1441571.
- Press, W.H., Teukolsky, S.A., Vetterling, W.T. & Flannery, B.P., 1992. *Numerical Recipes in FORTRAN: The Art of Scientific Computing*, Cambridge University Press, Cambridge.
- Rabben, T.E., Tjelmeland, H. & Ursin, B., 2008. Non-linear Bayesian joint inversion of seismic reflection coefficients, *Geophys. J. Int.*, **173**(1), 265–280, doi:10.1111/j.1365-246X.2007.03710.x.
- Sato, T., Kodaira, S., Takahashi, N., Tatsumi, Y. & Kaneda, Y., 2009. Amplitude modeling of the seismic reflectors in the crust-mantle transition layer beneath the volcanic front along the northern Izu-Bonin island arc, *Geochem., Geophys., Geosys.*, **10**, Q02X04, doi:10.1029/2008GC001990.
- Tessmer, G. & Behle, A., 1988. Common reflection point data-stacking for converted waves, *Geophys. Prospect.*, **36**(7), 671–688, doi:10.1111/j.1365-2478.1988.tb02186.x.
- Thomsen, L., 1999. Converted-wave reflection seismology over inhomogeneous, anisotropic media. *Geophysics*, **64**(3), 678–690, doi:10.1190/1.1444577.
- Veire, H.H. & Landrø, M., 2006. Simultaneous inversion of PP and PS seismic data, *Geophysics*, **71**(3), R1–R10, doi:10.1190/1.2194533.
- Wang, Y. & Singh, S.C., 2003. Separation of P- and S-wavefields from wide-angle multicomponent OBC data for a basalt model, *Geophys. Prospect.*, **51**(3), 233–245, doi:10.1046/j.1365-2478.2003.00377.x.
- Wang, Y., Singh, S.C. & Barton, P.J., 2002. Separation of P- and SV-wavefields from multi-component seismic data in the τ - p domain, *Geophys. J. Int.*, **151**(2), 663–672, doi:10.1046/j.1365-246X.2002.01797.x.
- Xu, Y. & Bancroft, J.C., 1997. Joint AVO analysis of PP and PS seismic data. In *CREWES Research Report*, volume 9, chapter 34, pages 1–44. University of Calgary.
- Yilmaz, Ö., 2001. *Seismic Data Analysis*, Vol. 10: Investigations in Geophysics, Society of Exploration Geophysicists, Tulsa.
- Zhang, J. & Mancini, F., 2006. PP and PS joint inversion—a case study from West Africa, in *68th EAGE Conference and Exhibition*, Vienna, Austria. European Association of Geoscientists and Engineers. P298.
- Zoeppritz, K., 1919. Erdbebenwellen VII b: über Reflexion und Durchgang seismischer Wellen durch Unstetigkeitsflächen, *Nachrichten von der Gesellschaft der Wissenschaften zu Göttingen, Mathematisch-Physikalische Klasse*, **1919**, 66–84.
- Zoeppritz, K., Geiger, L. & Gutenberg, B., 1912. Erdbebenwellen V: Konstitution des Erdinnern, erschlossen aus dem Bodenverrückungsverhältnis der einmal reflektierten zu den direkten longitudinalen Erdbebenwellen, und einige andere Beobachtungen über Erdbebenwellen, *Nachrichten von der Gesellschaft der Wissenschaften zu Göttingen, Mathematisch-Physikalische Klasse*, **1912**, 121–206.
- Zollo, A. et al., 2003. Evidence for the buried rim of Campi Flegrei caldera from 3-D active seismic imaging, *Geophys. Res. Lett.*, **30**(19), 2002, doi:10.1029/2003GL018173.
- Zollo, A., Maercklin, N., Vassallo, M., Dello Iacono, D., Virieux, J. & Gasparini, P., 2008. Seismic reflections reveal a massive melt layer feeding Campi Flegrei caldera, *Geophys. Res. Lett.*, **35**, L12306, doi:10.1029/2008GL034242.